Scalable hierarchical wood/ZnO nanohybrids for efficient mechanical energy conversion

Ying Gao [a,b], Farsa Ram [b], Bin Chen [b], Jonas Garemark [b], Lars Berglund [b], Hongqi Dai [a,*], Yuanyuan Li [b,*]

[a] *Jiangsu Co-Innovation Center of Efficient Processing and Utilization of Forest Resources, Nanjing Forestry University, Nanjing 210037, China*
[b] *Wallenberg Wood Science Center, Department of Fiber and Polymer Technology, KTH Royal Institute of Technology, SE-10044 Stockholm, Sweden*

HIGHLIGHTS

- In situ synthesis of hierarchical 3D array of multilayered ZnO inside wood.
- Highly charged wood enables multilayered ZnO synthesis without seeding.
- Wood/ZnO composites are efficient for piezoelectric mechanical energy conversion.
- The output voltage is 1.5 V with output current of 2.91 nA and power density of 2.91 nW/cm^2.

GRAPHICAL ABSTRACT
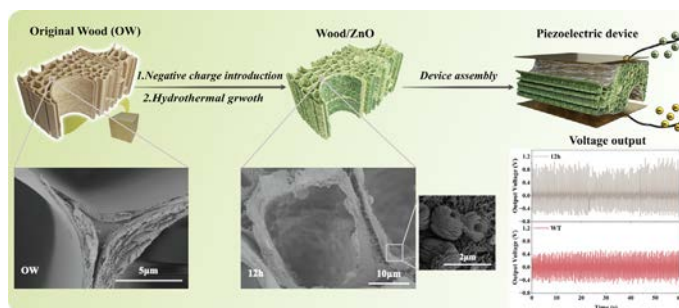
ARTICLE INFO

ABSTRACT

Owing to the hierarchical structure, easy multi-functionalization and favorable mechanical properties, wood could harvest electricity from mechanical energy through piezoelectric behavior. In this work, a scalable method to synthesize wood/ZnO composite with multilayered ZnO morphologies is reported for efficient mechanical energy conversion. The synthesis includes charged wood template fabrication, precursor infiltration, and ZnO hydrothermal growth, resulting in controlled ZnO morphologies and distributions while maintaining the hierarchical structure of the wood. Stereo-digital image correlation (stereo-DIC) investigated the relationship between deformation and piezoelectric performance, which revealed the homogeneous distribution of multilayered ZnO enhance piezoelectric performance. The output voltage of wood/ZnO was 1.5 V under periodic mechanical compression (8–10 N) for 300 cycles, while the output current was 2.91 nA. The scalable synthesis strategy and piezoelectric performance are significant for the design of advanced wood nanocomposites for sustainable and efficient energy conversion systems.

1. Introduction

Wood is taking an important and increasing role in sustainable energy harvesting such as solar to water energy conversion through solar steam generation [1], mechanical to electricity conversion through piezoelectric effect [2,3], and heat to electricity conversion [4,5]. Among a various forms of renewable energy resources, harvesting mechanical energy through wood has huge potential due to the favorable mechanical properties and easy chemical functionalization [3,6,7]. Piezoelectric mechanical energy conversion is an attractive approach for mechanical energy harvesting. The potential for wood as a biobased piezoelectric material is intriguing, which the displacement of the crystalline cellulose from cell wall resulted the piezoelectric properties [8,9]. However, the composed non-piezoelectric lignin and hemicellulose inside

* Corresponding authors.
  E-mail addresses: hgdhq@njfu.edu.cn (H. Dai), yua@kth.se (Y. Li).

native wood lead to low piezoelectric constant (0.03–0.1 pC/N) [8]. Modifying wood substrates through wood nanotechnology provides more opportunities for extending wood piezoelectric performance.

By using delignification to increase cellulose content and wood crystallinity, delignified wood showed an increased output voltage of 0.84 V from 0.0081 V [6]. Removing lignin and hemicellulose by fungi degradation resulted in further enhanced elastic compressibility, leading to a higher output voltage up to 0.87 V [10]. Despite the current achievements by wood modification, there are issues with either low efficiency due to weak piezoelectric response of wood (cellulose) or unfavorable processing that takes few weeks. Combing with high piezoelectric inorganic nanoparticles offers possibilities for higher power output [11]. ZnO is often investigated ascribing to its high piezoelectric property and easy fabrication with controlled morphology [12]. However, a based material is required due to the poor compressibility and easy aggregation of ZnO. Ram et al. fabricated wood/ZnO composites through ZnO nanoengineering on the wood surface showed an optimum voltage of 1.3–1.4 V [6]. ZnO inserting the bulk structure can combine advantages of wood structure and properties of ZnO in a better way compared with surface coating.

Depositing as-prepared ZnO nanoparticles into the wood structure is often used to decorate bulk wood [13–15]. Nanoparticle accumulation and challenges with nanoparticle diffusion into the interior structure of the wood are difficulties. In situ formation of nanoparticles offers processing advantages [16], although morphology control of those nanoparticles is challenging. Ming *et al.* reported wood/ZnO nanohybrids by sol–gel seeding on wood surface/inside the wood, followed by ZnO nanostructures growth *via* carbonization [17]. Carbonization resulted in a rigid sample while cellulose was pyrolyzed. Hydrothermal synthesis into the bulk wood is another main strategy while seeding process is often necessary [6]. Seeding normally is repeated multi times to ensure enough loading of Zn precursor, which is time consuming and usually leads to wood structure shrinkage or even collapse. In addition, ZnO with a multilayer structure (such as nanospheres, nanorods, nanoleaves, nanodisks, or nanoflowers) can enhance the contact

between particles, exert a strong influence on their energy conversion performance [19]. This provides motivation for the development of facile methods for ZnO precipitation in wood with ZnO multilayer morphologies.

In this work, new strategy was proposed for ZnO synthesis in wood by introducing negative charge to wood template (WT) followed by hydrothermal growth (Fig. 1). The accessibility of wood to Zn^{2+} ions was first improved by increasing wood porosity and surface charge through delignification combined with periodic acid oxidation. Consequently, Zn^{2+} ions can quickly diffuse into the highly negatively charged wood and combine with negatively charged carboxyl groups or aldehyde. Followed by the hydrothermal growth, multilayered ZnO uniformly distributed in wood were obtained with controllable morphology and content by tailoring the growth time. Compared with the literature, normal seeding step in conventional ZnO growth was eliminated, which induces wood structure collapse/shrinkage. In addition, charge controlled Zn^{2+} ions adsorption enables ZnO decoration not only in the cell lumen, but also inside the cell wall, which was not reported in literature. Stereo-digital image correlation (stereo-DIC) is used to monitor the surface deformation of these samples [18,19] and investigate the relationship with piezoelectric performance, which is rarely reported for wood piezoelectric energy conversion. Aiming for high piezoelectric output with the ZnO embedded, a 1.5 V voltage output was realized. Moreover, the wood/ZnO provides a new idea for the natural structure of wood for mechanical energy harvesting and conversion.

2. Experimental section

2.1. Wood delignification

Balsa wood (Ochroma pyramidale, purchased from Wentzels Co. ltd., Sweden) blocks with a density of 110 ± 2 kg/m³ were cut into 1 cm × 1 cm × 1.5 cm (tangential × radial × axial) cuboids. Delignification was conducted by wood treatment in 1 wt% sodium chlorite (NaClO₂, Sigma-Aldrich, Sweden) solution with constant
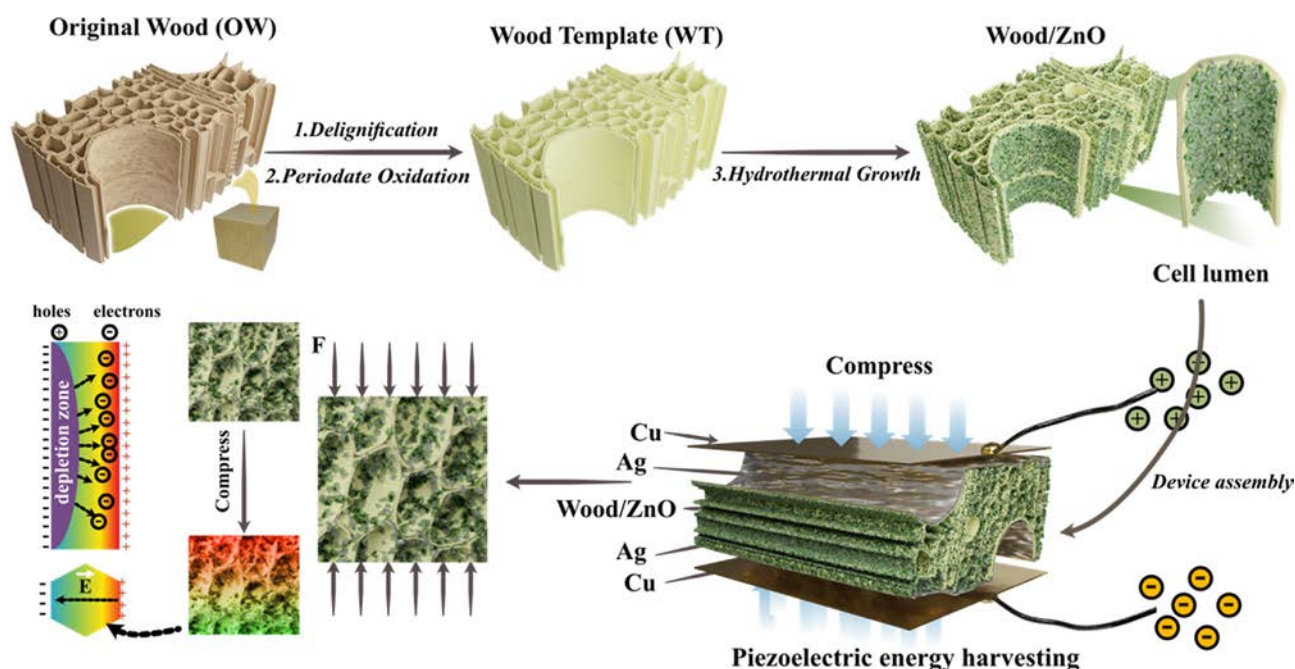

Fig. 1. Schematic representation of wood/ZnO synthesis method with lumen uniformly decorated by multilayered ZnO and the illustration of using the wood/ZnO for piezoelectric energy harvesting.

pH at 4.6 through acetate buffer under 80 °C. The reaction was performed until the samples became completely white. After that, the delignified wood (DW) was washed using deionized water (DIW) for several times to remove residual chemicals.

2.2. Preparation of wood template (WT) by periodate oxidation

DW was further oxidized by sodium periodate to increase the surface charge [20]. DW was put into a 250 ml beaker with 100 ml of DIW and 0.41 g of $NaIO_4$ ($NaIO_4$, Sigma-Aldrich, Sweden). The beaker was then covered with aluminum foil to prevent the photo-induced decomposition of periodate. The reaction was performed by stirring the mixture with a magnetic stirrer in a water bath at 75 °C for 2 h. After that, the WT was washed several times with DIW to remove iodine-containing compounds. Then the WT was stored in DIW.

2.3. Hydrothermal growth of ZnO nanoparticles inside WT

The hydrothermal reaction was performed to grow ZnO inside WT. Before synthesis, a water solution of 0.4 M zinc nitrate hexahydrate ($Zn(NO_3)_2 \cdot 6H_2O$, Sigma-Aldrich, Sweden) and 0.4 M hexamethylenetetramine (HMTA, $(CH_2)_6N_4$, Sigma-Aldrich, Sweden) was prepared under vigorous stirring at room temperature until it became transparent respectively. The wood templates were immersed into the 0.4 M $Zn(NO_3)_2 \cdot 6H_2O$ solution for 1 h under vacuum. After that, an equimolar 0.4 M HMTA was added. The WT containing solutions was then transferred into an autoclave for hydrothermal growth at 95 °C for 6 h, 12 h, and 24 h, respectively. Finally, the wood/ZnO were washed several times with DIW to remove residual chemicals followed by freeze-drying.

2.4. Piezoelectric energy harvesting

To fabricate a mechanical energy harvester or piezoelectric nanogenerator (PENG), the WT and wood/ZnO 12 h ($1 \times 1 \times 1.5$ cm³, T × R × L) were then coated with silver paste on top and bottom along the fiber direction and dried in the oven at 80 °C for 2 h. Further, conductive copper tapes were pasted on the silver-coated surface and soldered a set of copper wires for the output measurements. The piezoelectric performances were investigated by measuring peak to peak output voltage and current under a cyclic load. The cyclic load of 8–10 N was applied using a Linear motor (Linmot, USA) and it was tracked using a Flexi force ELF system (Tekscan, USA). Keithley's DMM 7510 was used to record the output voltage and current. The power density can be calculated using the following Eq.:

$$Power density = \frac{VxI}{Area}$$

where V and I are the output voltage and current, respectively. The digital photo of the piezoelectric nanogenerator mounted on the linear motor setup is shown in Fig. 2a and 2b. We have also added a simpler schematic of the device in Fig. 2c.

2.5. Digital image correlation (DIC) for stress transfer

The interaction of mechanical behavior and piezoelectricity performance of wood/ZnO was studied using stereo-digital image correlation (stereo-DIC). Cubic wood/ZnO 6 h, wood/ZnO 12 h and wood/ZnO 24 h samples with a nominal dimension of $10 \times 10 \times 10$ mm³ were prepared and painted with black speckles. These samples were then loaded vertical to the fiber direction by a universal testing machine (Instron E1000). The samples were periodically compressed with an amplitude of 0.5 mm and frequency of 2 Hz for 25 or 50 cycles. The loading progress of these samples
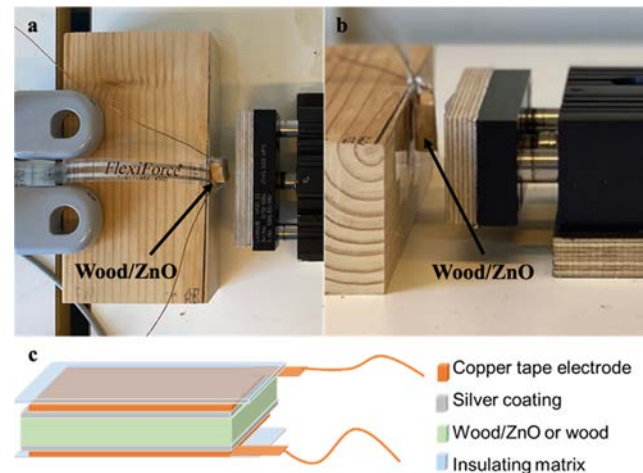

Fig. 2. Wood/zno device loaded on the linear motor setup: a) to-view, b) side-view, and c) schematic illustration of the device.

was recorded by the stereo-digital image correlation (stereo-DIC) system with Basler acA4096-30um cameras (resolution of 4096×2168 pixels). The images were captured with a frame rate of 20 Hz. The piezoelectricity of the samples was also measured simultaneously by pasting conductive copper tapes on the silver-coated surface. Processing the images using VIC-3D (Correlated Solutions, USA) leaded to the strain distribution on the sample surfaces. To this aim, subset size of 101×101 pixels, step size of 3 pixels and strain window size of 15×15 pixels were specified in DIC measurements.

2.6. Characterization

The morphologies of the samples were observed with a Field-Emission Scanning Electron Microscope (FE-SEM, Hitachi S-4800, Japan) operating at an acceleration voltage of 3 kV. Pt/Pd coating was sputtered on the samples for 40 s before characterization. Thermogravimetric analysis (TGA, Mettler Toledo- TGA/DSC 1, America) was performed to measure the ZnO loading at a heating rate of 10 K/min from room temperature to 800 °C under O_2 flow of 50 ml/min. Wood was fully carbonized and decomposed after 300 °C under O_2 while ZnO was stable even under 800 °C [13]. Therefore, the weight percentage increase above WT at 800 °C is taken into account as the ZnO content. ZnO crystal structure was performed by X-ray diffraction (XRD, PANalytical-X'Pert PRO, Netherlands) in a powder diffractometer under 40 mA and 45 kV. The scan interval was 5° < 2θ < 70°, with a step size of 0.03° (2θ). The crystallinity index (CrI) was calculated according to Eq. based on the Segal method [21]:

$$CrI = \frac{I_{002} - I_{am}}{I_{002}}$$

where I_{002} is the intensity of crystallized regions at peak intensity (2θ = 22.5°), and I_{am} is the amorphous regions at peak intensity (2θ = 18°). To analyze the influence of growth time on ZnO crystal size, the average grain size of ZnO was estimated by Scherrer's equation [22]:

$$D = \frac{K\lambda}{\beta \cos \theta}$$

where D is the average diameter of ZnO nanoparticles, λ represents the X-ray wavelength (0.154 nm), K refers to the Scherrer constant (0.89), β is the full width of the peak at half maximum (FWHM), and θ represents the Bragg diffraction angle. The average diameter of ZnO nanoparticles in ZnO/Wood was calculated using the character-

istic peaks {1 0 0}, {0 0 2} and {1 0 1}. Fourier-transform infrared spectroscopy (FTIR) spectra was obtained at 16 scans and a resolution of 4 cm^{-1} in transmission mode with a Spectrum 100 FT-IR Spectrometer (Perkin Elmer, UK). The scan range was fixed between 400 and 4000 cm^{-1}. Surface charge density was measured by conductive titration (856 Conductimeter Module, Metrohm). The wood samples were pretreated, dried and ground into powder for testing. The balsa powder was first protonated using HCl (0.1 M, 5 ml). Then titration was performed using NaOH (0.05 M). When the conductance decreased till the equivalence point, the charge density was calculated according to the NaOH consumption. The Brunauer-Emmett-Teller (BET) specific surface area was evaluated by nitrogen physisorption. Before the nitrogen adsorption, 0.1 g of material was degassed at 90 °C for 2 days, followed by the subsequent BET analysis. The analysis was carried out at −196 °C under a relative vapor pressure of 0.05–0.25 with a Micromeritics ASAP 2020. The BET specific surface area was calculated from the attained isotherms. Finally, electrical conductivity was measured using an Ossila four-point probe system. The compressive test was performed on a universal testing machine (Instron 5944, UK) at ambient condition (25 °C and 50 % RH). All the measurements were performed using 1 cm × 1 cm × 1.5 cm (tangential × radial × axial) samples, with a 500 N load cell. The test for different maximum strains were performed at a strain rate of 5 % min^{-1}.

3. Results and discussion

3.1. The synthesis of wood/ZnO nanohybrids

Early method developments using neat wood were not able to produce the desired flower morphology of ZnO particles and load-

ing, possibly due to insufficient Zn^{2+} adsorption (**Fig. S1a**, **Fig. S1b** **and Table S1**). Results improved slightly using delignified wood substrates, although very few ZnO particles with nanosphere morphology were formed (**Fig. S1c** and **Fig. S1d**). To homogeneously decorate wood with multilayered ZnO, periodate oxidation was performed on delignified wood. Fig. 3**a** illustrates the wood structure change during the chemical pre-treatment. Delignification (around 22 wt% lignin removal), leads to increased nanoporosity, enhanced specific surface area (SSA), and improved cell wall accessibility [23–25]. Fig. 3**b and 3c** show the pore generation inside cell wall after delignification. The disappearance of the FTIR peak at 1500 cm^{-1}, which is attributed to aromatic skeleton vibrations from lignin, further confirmed the removal of lignin (Fig. 3**e**). During the reaction, part of the polysaccharides was oxidized to carboxylic groups, leading to wood surface charge increase from 25.9 μeq/g (original wood, OW) to 241.3 μeq/g, which is beneficial for Zn^{2+} adsorption. However, no ZnO could be obtained by using DW and the ZnO coverage density is low (**Fig. S1c** and **Fig. S1d**). To further enhance Zn^{2+} adsorption, periodate oxidation was then performed, resulting in wood template (WT) for ZnO growth. After periodate oxidation, vicinal hydroxyl groups at carbon atoms 2 and 3 in an anhydroglucose unit of cellulose were converted to two aldehyde groups (**Fig. S2**) [20]. The appearance of the FTIR peak at around 1640 cm^{-1} (characteristic peak for aldehyde carbonyl group) along with a strengthening of the band at 895 cm^{-1} (Fig. 3**e**), assigned to the hydrated forms of aldehyde groups, confirming the successful oxidation of wood [26]. The surface charge of WT increased to 588.9 μeq/g, leading to enhanced Zn^{2+} adsorption capacity (**Fig. S3**). The XRD spectra (Fig. 3**f**) of all samples show clear peaks of native cellulose I crystalline structure at around 14.7°, 16.5°, and 22.5°. The cellulose crystallinity slightly
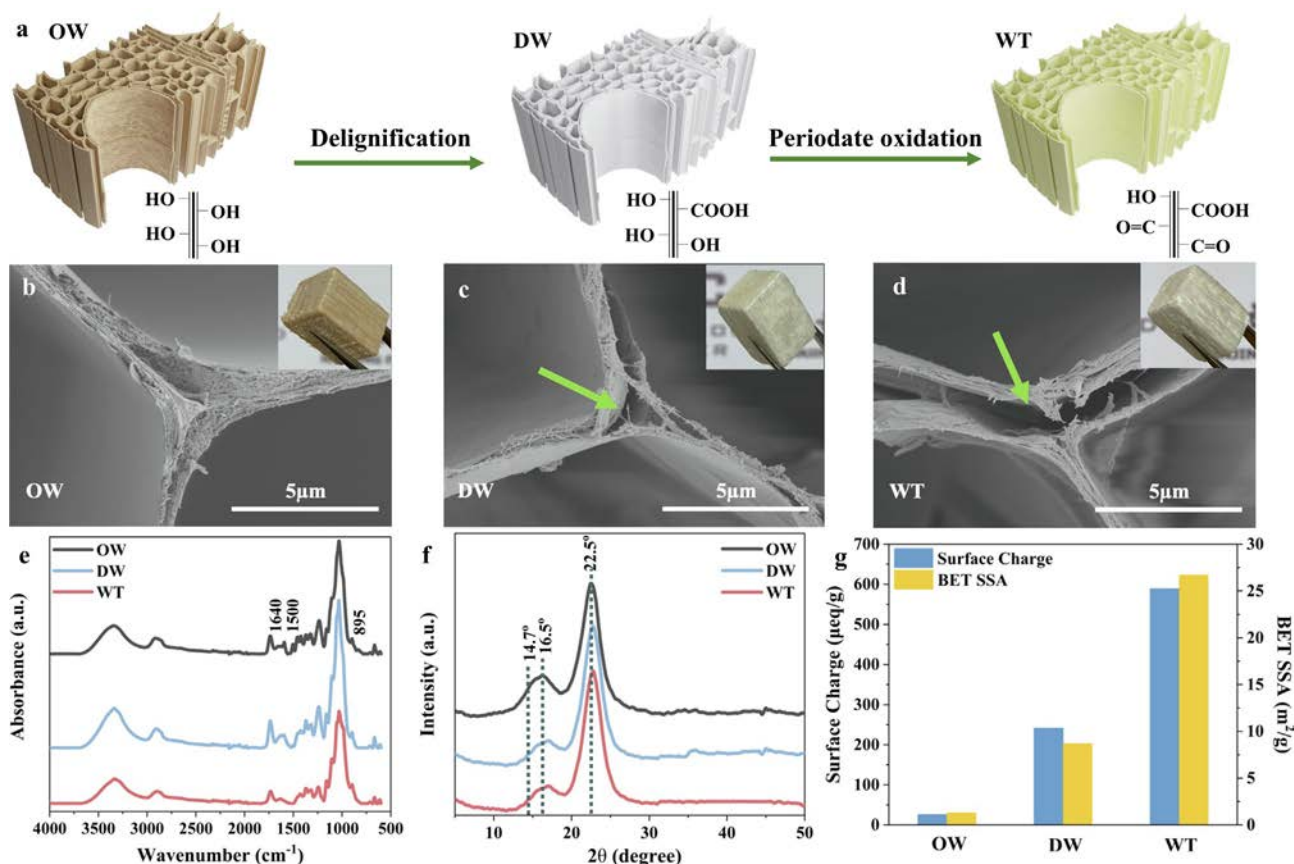

Fig. 3. (a) Schematic of the wood template preparation method. Cross-sectional SEM images of (b) OW, (c) DW and (d) WT. Inset images are photographs of the OW, DW, and WT respectively. (e) FTIR spectra of OW, DW and WT. (f) XRD patterns of OW, DW and WT. (g) Surface charge and BET SSA data of OW, DW and WT.

increased from OW (69.4 %) to delignified wood (DW, 74.3 %) mainly due to the removal of lignin and part of hemicellulose. For WT, the crystallinity was 66.2 %, lower than DW due to the periodate oxidation. It should be noted that the macrostructure of wood is preserved after the pre-treatment, as shown from the SEM images and photographs in Fig. 3c, 3d, S4a, and S4b. An increased SSA of WT with value of 26.7 m^2/g was observed from 1.3 m^2/g of OW. This is mainly due to the generation of nano and submicron pores in the cell wall (Fig. 3b, 3c, and 3d) ascribing to lignin removal and partial polysaccharide degradation (15.3 wt% during oxidation).

Hydrothermal growth was conducted on WT to get ZnO inside wood. After hydrothermal growth for 6 h, a layer of loose multilayered ZnO formed on the cell lumen (Fig. 4a, 4d, 4g). The ZnO showed a diameter of around 0.5 μm consisting of 10–15 ZnO flake layers (Fig. 4d). Such ZnO morphology is beneficial for mechanical energy conversion [27]. With growth time of 12 h, the multilayered ZnO diameter increased to 1–2 μm with more ZnO nanoflake layers (Fig. 4e). Higher ZnO coverage density is apparent (Fig. 4b, 4e, 4h). After 24 h growth, coverage density is further enhanced yet the original flower-like structure disappeared (Fig. 4c, 4e, 4f). One hypothesis is that with increased growth time, the particle density at the surface changed, leading to the surface energy variation, resulting in particles partial diffusion and re-precipitation without hierarchical microflower structure [28]. The morphology change indicates the ZnO morphology controllability during nanoparticles

formation, which is challenging for bulk wood decoration. The appearance of the wood/ZnO is similar to WT as shown in Fig. 4b. The wood macrostructure is preserved but decorated with ZnO nanoparticles as shown in the low magnification SEM images (Fig. 4g, 4h, and 4i). Zn-based elemental mappings confirm the homogenous coverage of ZnO on the lumen surface (Fig. S4c, S4d, S4e). This type of wood/ZnO with uniform distribution of high concentration multilayered ZnO inside wood is rarely reported. Table S1 presents the literature summary of the wood/ZnO hybrids.

3.2. The characterization of wood/ZnO nanohybrids

The ZnO content increased with the increased hydrothermal growth time revealed by TGA spectra (Fig. 5a). The ZnO loading was 9.0 wt% after 6 h growth and increased to 15.4 wt% after 12 h reaction. Further extended the growth time to 24 h, ZnO could cover the entire wood structure with a ZnO content of 17.2 wt%. To confirm the successful formation of the ZnO structure, FTIR spectra of the samples were collected (Fig. 5b). The peaks at the wavenumbers around 1310 cm^{-1} appeared in the spectra of wood/ZnO, corresponding to the asymmetric and symmetric stretching of zinc carboxylate at the surface of ZnO [29]. The intensity decreased at 1730 cm^{-1} corresponding to carbonyl group (C=O) and the intensity increased at 1600 cm^{-1} corresponding to carboxylate groups (–COO$^-$) compared with WT indicated the successful modification
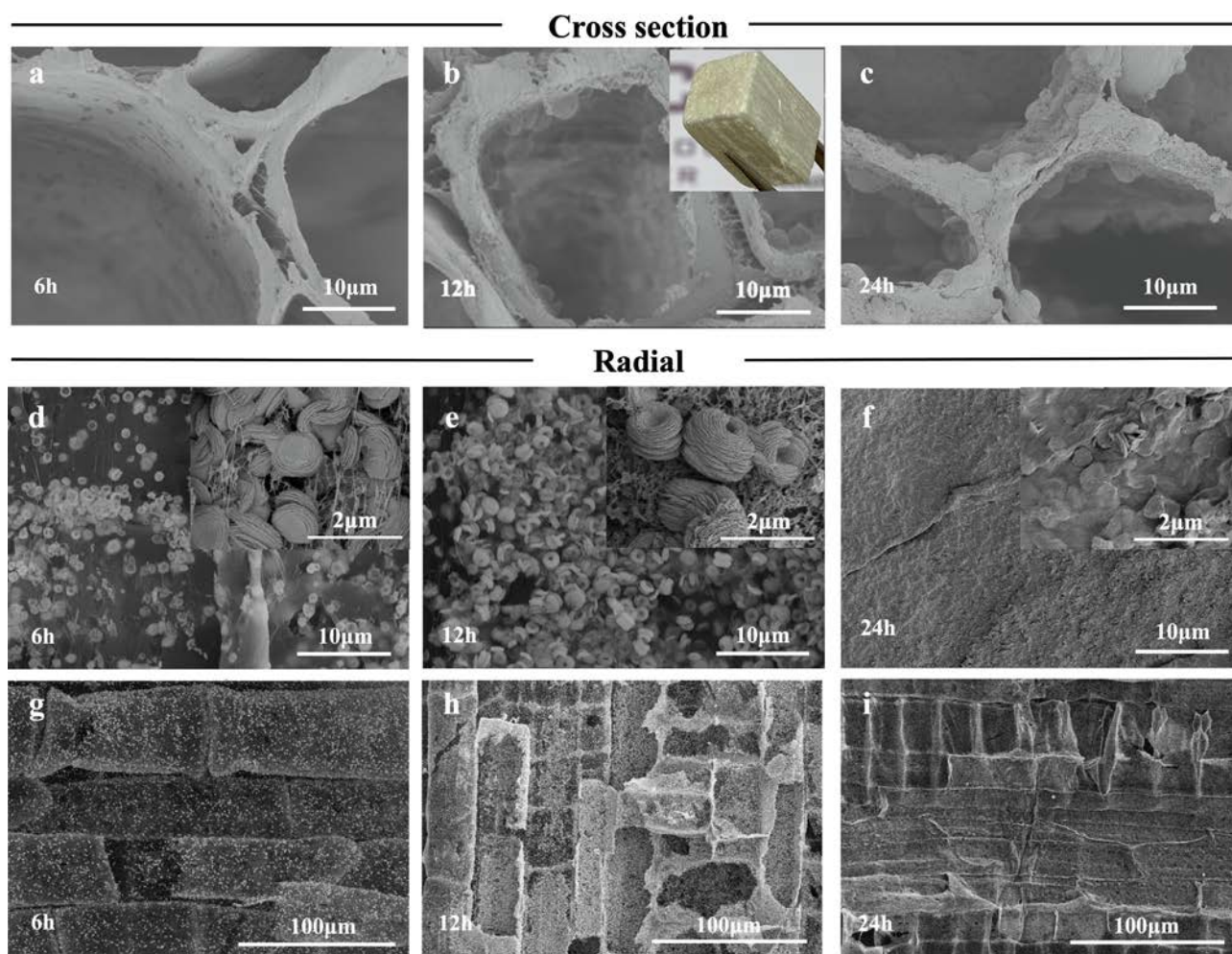

Fig. 4. Cross-sectional SEM images of wood/ZnO after hydrothermal treatment for (a) 6 h, (b) 12 h, and (c) 24 h. The inset image of (b) is a photograph of 12 h. (d), (e) and (f) are high-resolution radial face SEM images with different ZnO morphology after hydrothermal growth of 6 h, 12 h, and 24 h, respectively. Inset images are high-resolution SEM images, respectively. (g), (h) and (i) are the low-resolution radial face SEM images of different hydrothermal growth times of 6 h, 12 h, and 24 h.
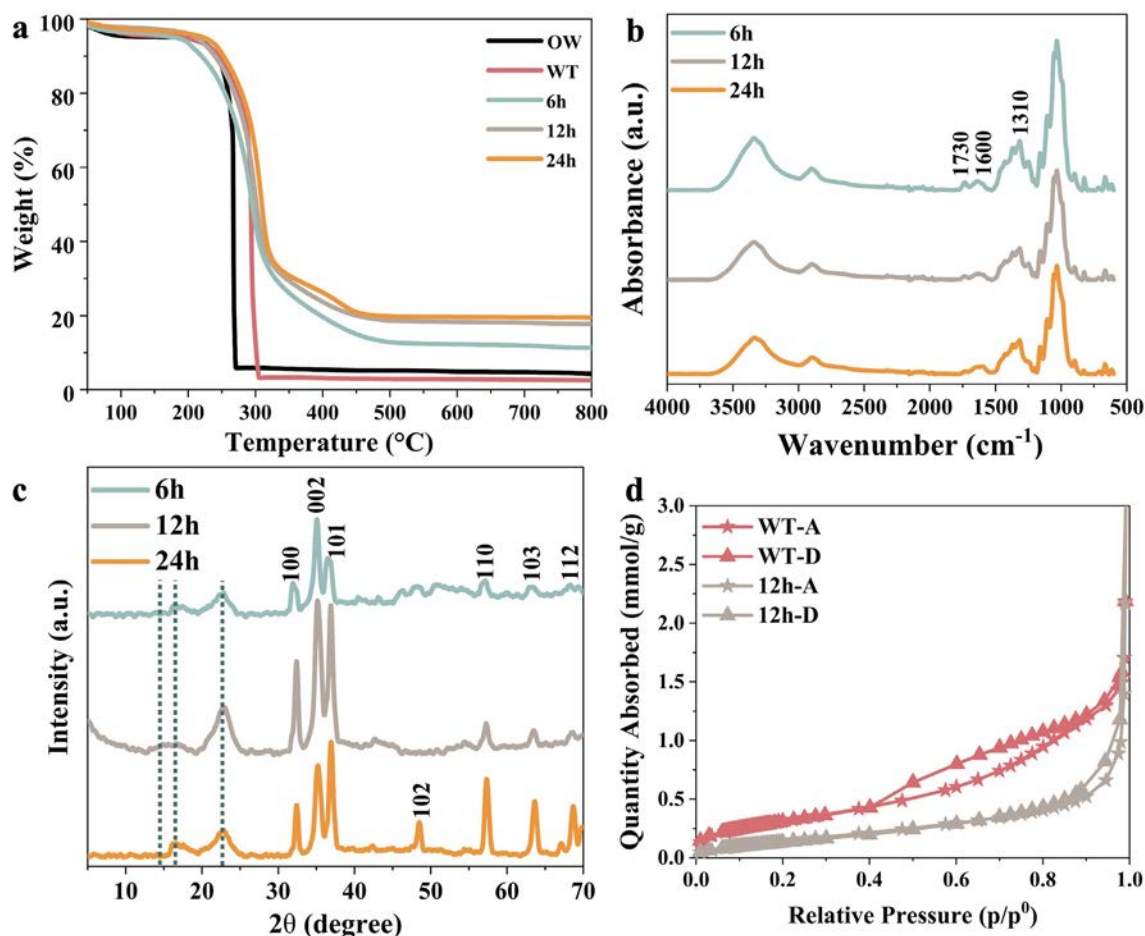
Fig. 5. (a) TGA curves (under O_2) of OW, WT and wood/ZnO (6 h, 12 h and 24 h). (b) FTIR spectra of wood/ZnO. (c) XRD patterns of wood/ZnO. (d) Nitrogen adsorption and desorption measurements of WT and wood/ZnO 12 h. A displays adsorption, whereas D symbolizes desorption.

and the bonding of carboxylate ions by Zn^{2+} [30]. One hypothesis for the formation of zinc carboxylate is the reaction between reactive ZnO nuclei and the hydroxyl groups in the system.

The XRD spectra of wood/ZnO also confirmed the successful formation of ZnO (Fig. 5c). All samples had peaks at around 14.7°, 16.5°, and 22.5°, indicating the preservation of cellulose I crystal structure. The sharp diffraction peaks at 32.3°, 35.3°, 36.7°, 48.5°, 57.3°, 63.6° and 68.7° attributed to wurtzite ZnO hexagonal structure (Wurtzite-type, JCPDS Card No. 75-0576), corresponding to the planes at {100}, {002}, {101}, {102}, {110}, {103} and {112} respectively. The average crystal sizes of ZnO were estimated to be 12.87 nm, 13.46 nm, and 12.83 nm corresponding to hydrothermal 6 h, 12 h, and 24 h. The decrease of ZnO crystal size of 24 h growth could be attributed to the ZnO dissolution and release back to the growth solution during the long reaction time [31]. This further supports the hypothesis of ZnO morphology change after 24 h growth. At the same time, according to the morphology of ZnO obtained by SEM, the multi-level structure of ZnO particles is not complete after hydrothermal growth for 6 h. However, the multi-level flower-like structure of ZnO particles in the 24 h sample has collapsed, and the ZnO flakes have fallen off from the flower-like structure and become a dense and disordered zinc oxide layer. This also leads to a reduction in the ZnO crystallite size. With the formation of ZnO inside the wood, the BET SSA decreased from 26.7 m^2/g for WT to 13.6 m^2/g for the wood/ZnO (12 h) (Fig. 5d). Hypothesis is that the formation of ZnO blocked part of the mesopores in the wood template and increased the density of hybrid.

Mechanical property of the material is critical to the piezoelectric performance. Compressive stress–strain curves were measured to evaluate all the samples. The samples were tested along the radial direction (Fig. 6a), transverse to fiber direction. WT showed lower initial Young's modulus (around 50 MPa) compared to OW (149 MPa) (Fig. 6b and 6c). The stress level during cycling to different strains is also lowered for WT. This is mainly due to the removal of lignin which is vital to the stiffness of the structure while periodate oxidation further weakens the structure by cell wall components removal (15.3 % weight loss) and charge introduction. The Young's modulus of wood/ZnO samples were 9.41 MPa, 11.25 MPa and 9.50 MPa respectively. The stress level during cycling was further decreased for wood/ZnO compared with that of WT. The reason is wood degradation during hydrothermal treatment. At a strain of 20 %, the stress was only 84 kPa for wood/ZnO 6 h, while a value of 47 kPa was observed for Wood/ZnO 12 h. For longer treatment time, 24 h, the ZnO was as high as 17.2 wt% and the stress level was increased during cycling. From an application point of view, the low bulk modulus elastically compressible materials are highly suitable for mechanical energy harvesting[32–34]. In our case, wood/ZnO 12 h composition shows good compressibility (**Fig. S5**), which could be an advantage for piezoelectric energy conversion. The challenges for fabrication of the sample involve in obtaining highly charged wood with mechanical robustness as well as efficient synthesis of large samples. Highly charged wood is beneficial for Zn^{2+} ions adsorption and ZnO synthesis. Yet delignification and periodic acid oxidation significantly decreased the wood mechanical property, making
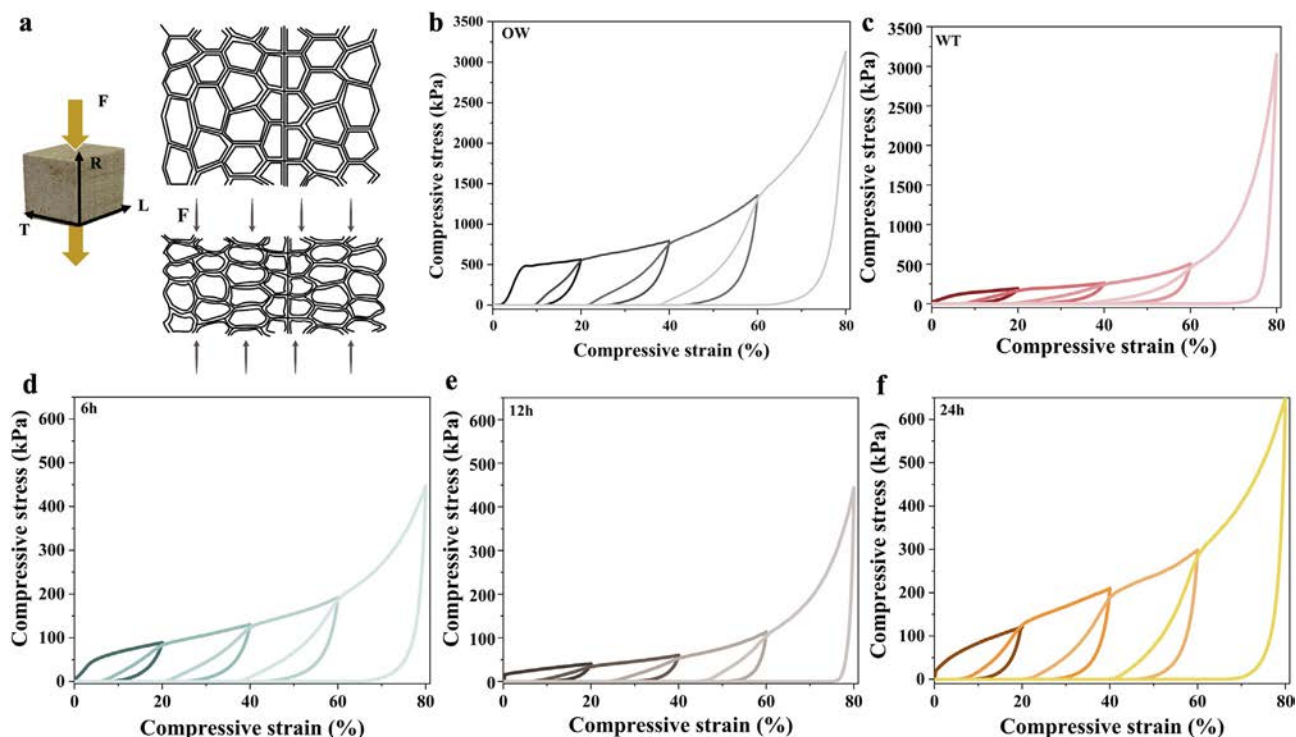
Fig. 6. Mechanical compression test of OW, WT, and wood/ZnO (6 h, 12 h, and 24 h). (a) Image of the test direction of all the samples and the skew of deformation of wood cells under loading in the radial direction. F is for the direction of compression force, R is for radial direction, T is for tangential direction, L is for longitudinal direction. Stress–strain curves of OW (b), WT (c), wood/ZnO 6 h (d), wood/ZnO 12 h (e) and wood/ZnO 24 h (f), with different maximum strains of 20 %, 40 %, 60 % and 80 %, respectively.

the handling of the sample during processing hard. Although enhanced apparently, mass diffusion inside large wood samples is still challenging (e.g. 10 cm × 10 cm × 1 cm). In addition, due to the differences between the wood interior and the synthetic environment (temperature difference, pH difference, concentration diffusion difference, etc.), how to achieve accurate regulation of the ZnO morphology inside the wood remains to be studied.

3.3. Digital image correlation (DIC) for stress transfer

Stereo-DIC is further used to monitor the strain distribution of these samples and investigate the relationship with piezoelectric performance. Fig. 7a-7c show the strain maps on the samples of wood/ZnO 6 h, wood/ZnO 12 h and wood/ZnO 24 h, respectively. The first column shows the strain maps with the peak loading value during the periodic loading progress, while the second column shows the strain maps with the minimum loading value during the periodic loading progress, respectively. It should be noted that each figure in Fig. 7 presents the strain distribution on two surfaces of a sample. The left surface is parallel to fiber direction, while the right part is vertical to the fibers. Unfortunately, the measured strain maps are quite noisy on the surfaces vertical to the fibers (left column) due to the unevenness of the sample surfaces. More information about the compression strain evolution for the three samples could be found in **Fig. S7, video S1, video S2** and **video S3**. When the wood/ZnO undergoes mechanical deformation, multilayer structure can increase the probability of contact between multilayered ZnO and thereby increase the probability of ZnO lattice deformation, leading to higher piezoelectric mechanical energy conversion. The piezoelectricity of the samples was measured simultaneously during strain mapping to investigate the correlation between sample deformation and piezoelectric performance (Fig. 7 the third column).

In the periodic loading progress, the majority part of the sample surface holds small elastic deformation, which can be recovered

(the first and second column in Fig. 7a-7c). The maximum compression strain at the maximum loading status increases with the ZnO growth time (see the lower limit of the color bar in the first column of Fig. 7a-7c). The strain concentration bands on the samples might be attributed to the combination of elastic buckling, plastic yielding and fracture [35], leading to a plateau on the stress–strain curve (Fig. 6). The elastic bucking is recoverable, and it initiates the elastic collapse of the walls when a critical load is reached. The plastic yielding of the walls happens when the moment on the cell wall exceeds the fully plastic moment, and then the plastic hinges and collapse show in the samples. The fracture might also be a reason, and the cell walls will be crushed when the moment acting on them exceeds a critical value.

The longer hydrothermal growth time results in larger damage in the samples. This will degenerate the performance of the walls to support compression loading, consequently leading to more significant strain concentration, that is the width of compression strain band and amplitude of the strain concentration increase with the growth time on the samples pointed in Fig. 7a-7c first column. This maybe the possible reason for the poor piezoelectric output in wood/ZnO with higher ZnO content (24 h) apart from ZnO nanostructure difference (Fig. 7 third column). Comparing wood/ZnO 12 h and wood/ZnO 6 h, though more damage shows in wood/ZnO 12 h sample, the piezoelectricity signal does not decrease correspondingly. This signifies the importance of specific geometry over the ZnO loading and homogeneous distribution of multilayered ZnO in wood/ZnO 12 h. The second compression strain maps on the samples of wood/ZnO samples were showed in **Fig. S6**.

For each kind of measurement, 3–5 devices were tested and representative data are presented in the manuscript. The output signals vary by 10–20 % within the same type of sample. The current signals have low noise to signal ratio. However, an FFT analysis of signals reveals that the wood/ZnO 6 h and 12 h have a dominant frequency around 2 Hz, which is similar to the loading
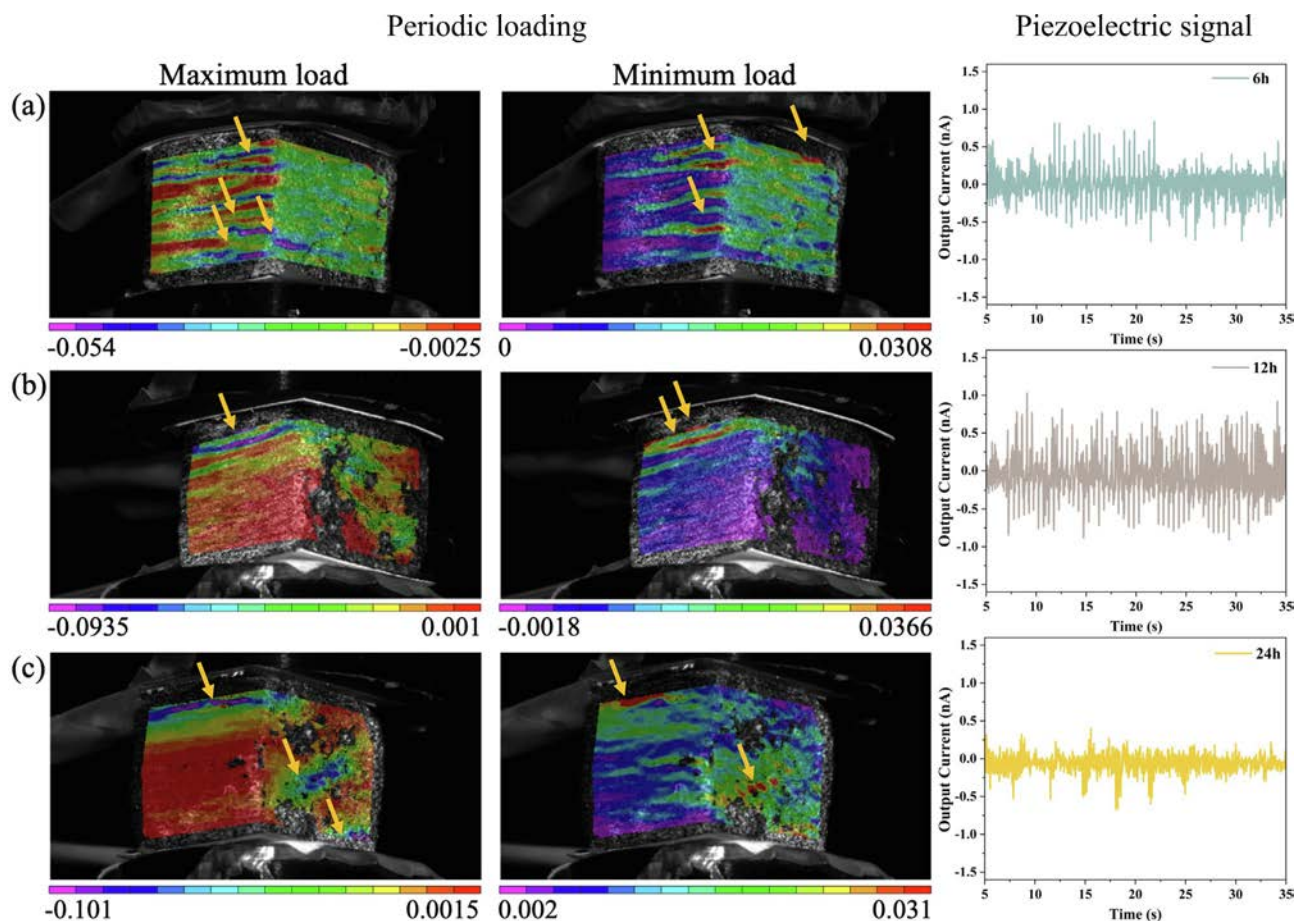
Fig. 7. The compression strain maps on the samples of (a) 6 h, (b) 12 h and (c) 24 h. The first two columns are the strain maps in the first periodic loading progress with maximum load and minimum load and the third column shows the corresponding piezoelectric current output signals under the periodic loading, the pointed position on the strain maps are the sample dagame point.

frequency, and they are indeed true signals (**Fig. S7**). In wood/ZnO 24 h, the dominant frequency is higher than the loading frequency, and the signals are mere noise.

3.4. Piezoelectric energy harvesting

Based on the results from mechanical and stereo-DIC tests and considering ZnO morphology and particle distribution, the Wood/ZnO 12 h was selected for further device assembly for mechanical energy conversion. Fig. 8**a** shows the schematic of the wood-based piezoelectric nanogenerator (PENG) and the working mechanism of multilayered ZnO. A record output voltage of 1.5 V was obtained (dimension of $15 \times 10 \times 10$ mm^3) for wood based PENGs (Fig. 8**b**) [2,3]. The peak to peak output voltage of wood/ZnO 12 h device has a standard deviation of ±0.21 V. The voltage signals are well above the noise level and there is minimal to no contribution from noise. Even the output voltage of WT based PENG (0.9 V) is higher than that of delignified balsa wood (0.84 V under 22.2 kPa, dimensions $15 \times 15 \times 14$ mm^3) [3], and fungal decayed elastic balsa wood (0.87 V under 10 N force, 45 kPa stress, dimensions $15 \times 15 \times 13.2$ mm^3) [2] reported in the literature. The possible reason is the high crystallinity (66.2 %) and good compressibility of WT. Introduction of ZnO with high piezoelectric constant (around 9.93 pm/V [36]) leading to further enhanced performance. The value is slightly higher than wood/ZnO where surface coating of ZnO was used (1.3–1.4 V), indicate the beneficial of bulk ZnO decoration. Output current was also increased for wood/ZnO 12 h based PENG (2.91nA, Fig. 8**c**) compared with that of the WT PENG

(0.45nA), 6.5 times higher. For wood/ZnO 12 h device, the power density was found to be 2.91 nW/cm^2 (calculated based on open circuit voltage and measured current), which is slightly higher than the previous wood aerogel-based device (0.6 nW/cm^2). Please note this value is calculated from two separate measurements of voltage and current without using any external resistor and may not reflect the true power density of the device, which is likely to be higher due to the presence of semiconducting ZnO (please see **Table S2**). The uniform distribution of ZnO, the crystalline Wurtzite ZnO structure, and good mechanical property are critical to the good performance. Wood/ZnO 12 h resulted in the highest output current (1.6 nA) due to two reasons: 1) ease of compressibility compared to 6 h and 24 h samples (lower resultant stress at fixed strain values as shown in Fig. 6**d-f**), 2) multilayered flower-like ZnO structures, which are poorly constructed in 6 h and dissolved in 24 h sample (refer SEM images). Additionally, the 6 h sample has a lower content of ZnO compared to the 12 h sample and resulted in an output current of 1.2 nA. In the 24 h sample, the longer growth time destroys the original multilayer structure and resembles a bulk ZnO film-like coating, making it less deformable compared to wood/ZnO 12 h sample, and hence signals were within noise level. For the piezoelectric performance, we tested all the samples for ~300 cycles where the piezoelectric performance had no significant reduction (Fig. 8**b**). This could be ascribed to the good compressibility of the wood/ZnO (Fig. 8**e**) and the strong adherence of multilayered ZnO to the wood structure (Fig. 4**e**). The wood scaffold offers mechanical support as it consists of a structural material of high strength. Under cyclic compression the wood
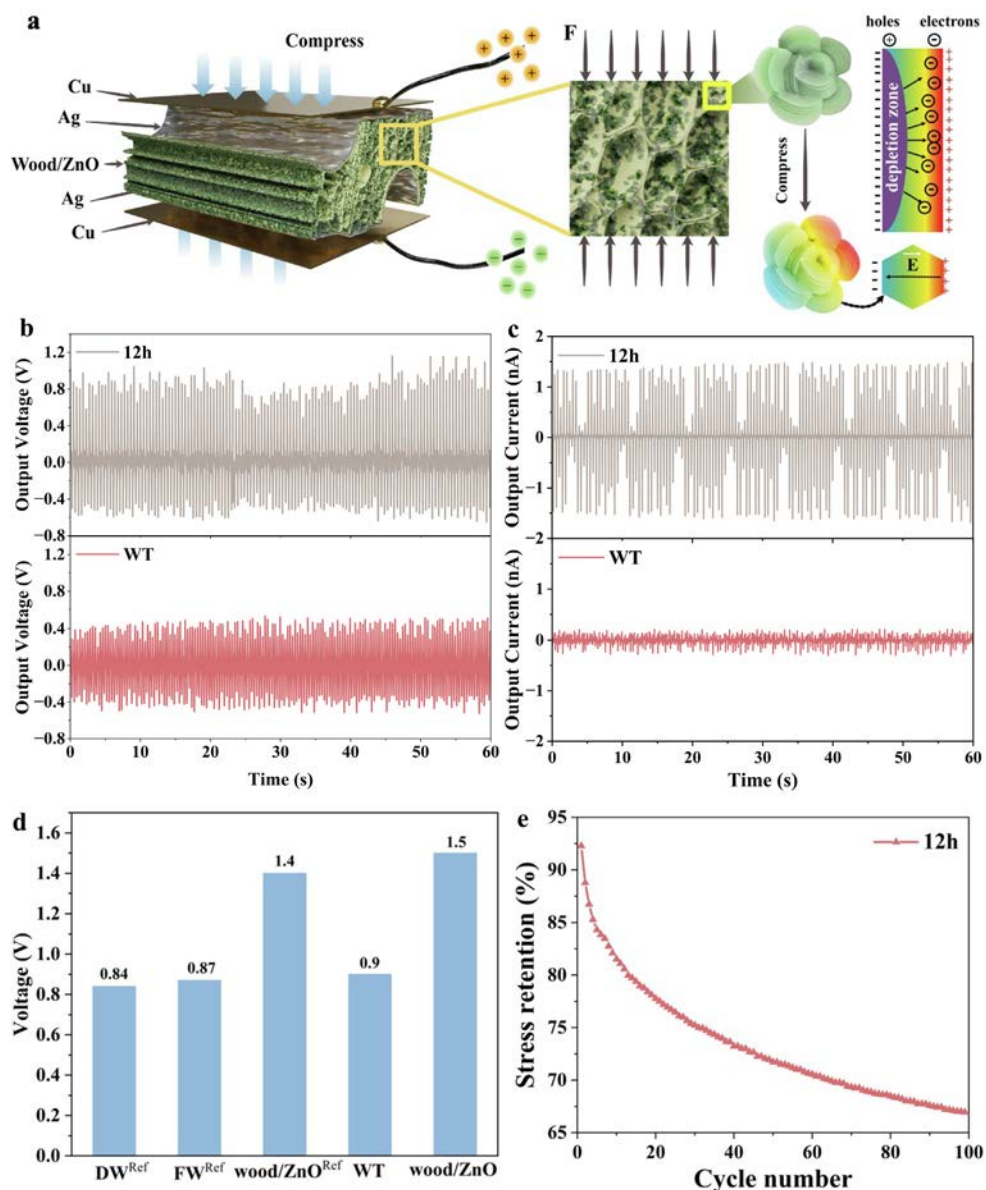
Fig. 8. Wood/ZnO for energy conversion. (a) Schematic of piezoelectric energy harvesting. F is mechanical force, E is for element simulation of the strain distribution along the multilayered ZnO when it is compressed; (b) The voltage output of WT and wood/ZnO (12 h) for around three hundred cycles; (c) The current output of WT and wood/ZnO (12 h) for around three hundred cycles; (d) The voltage output of different wood-based piezoelectric nanogenerators (the data of delignified wood [3], fungal wood [2] and wood/ZnO [6] are from literature); (e) Elastic strength retentions during 100 compressing/releasing cycles of wood/ZnO 12 h at a constant strain of 20 %.

structure insure effective transfer to the tightly bound ZnO structure, resulting in a sustainable electrical output from the composite.

4. Conclusion

In this work, a facile method for wood/ZnO with multilayered ZnO (0.5–2 μm in size) in Wurtzite crystalline from uniformly distributed throughout the wood template structure is presented, favorable for mechanical energy conversion. The highly charged wood template is important since it ensures high loading and uniform distribution of Zn^{2+}, leading to the elimination of any seeding step which induces shrinkage/collapse of the wood structure. The obtained wood/ZnO is efficient for piezoelectric energy harvesting influenced by ZnO morphologies, crystal structure, distribution in wood structure, as well as the hybrid materials mechanical performance. To investigate the relationship between strain distribution and piezoelectric performance, DIC showed the strain maps during the periodic loading progress. With the homogeneous distribution and higher loading of ZnO, wood/ZnO showed advantageous piezoelectric performance. Wood/ZnO 12 h ($1 \times 1 \times 1.5$ cm^3, tangential × radial × axial) resulted in output voltage up to 1.5 V with stable performance up to 300 cycles with a output current of 2.91 nA. The reported method is scalable and offers potential for wood-mineral nanohybrids design for piezoelectric applications in mechanical energy storage and conversion.

CRediT authorship contribution statement

Ying Gao: Conceptualization, Methodology, Data curation, Investigation, Writing – original draft. **Farsa Ram:** Methodology, Data curation, Investigation. **Bin Chen:** Methodology, Data curation, Investigation. **Jonas Garemark:** Drawing. **Lars Berglund:** Writing – review & editing. **Hongqi Dai:** Conceptualization, Writing – review & editing, Supervision. **Yuanyuan Li:** Conceptualization, Writing – review & editing, Supervision.

Data availability

Data will be made available on request.

Declaration of Competing Interest

The authors declare that they have no known competing financial interests or personal relationships that could have appeared to influence the work reported in this paper.

Acknowledgements

Appendix A. Supplementary data

Supplementary data to this article can be found online at https://doi.org/10.1016/j.matdes.2023.111665.

References

[1] M. Zhu, Y. Li, G. Chen, F. Jiang, Z. Yang, X. Luo, Y. Wang, S.D. Lacey, J. Dai, C. Wang, C. Jia, J. Wan, Y. Yao, A. Gong, B. Yang, Z. Yu, S. Das, L. Hu, Tree-Inspired Design for High-Efficiency Water Extraction, Adv. Mater. 29 (2017) 1–9, https://doi.org/10.1002/adma.201704107.

[2] J. Sun, H. Guo, G.N. Schädli, K. Tu, S. Schär, F.W.M.R. Schwarze, G. Panzarasa, J. Ribera, I. Burgert, Enhanced mechanical energy conversion with selectively decayed wood, Sci Adv. 7 (2021) 1–8, https://doi.org/10.1126/sciadv.abd9138.

[3] J. Sun, H. Guo, J. Ribera, C. Wu, K. Tu, M. Binelli, G. Panzarasa, F.W.M.R. Schwarze, Z.L. Wang, I. Burgert, Sustainable and biodegradable wood sponge piezoelectric nanogenerator for sensing and energy harvesting applications, ACS Nano 14 (2020) 14665–14674, https://doi.org/10.1021/acsnano.0c05493.

[4] Y. Li, J. Cui, H. Shen, C. Liu, P. Wu, Z. Qian, Y. Duan, D. Liu, Useful spontaneous hygroelectricity from ambient air by ionic wood, Nano Energy 96 (2022), https://doi.org/10.1016/j.nanoen.2022.107065.

[5] H. Sun, T. Ji, H. Bi, M. Xu, L. Cai, M. Manzo, Synergistic effect of carbon nanotubes and wood-derived carbon scaffold on natural rubber-based high-performance thermally conductive composites, Compos. Sci. Technol. 213 (2021), https://doi.org/10.1016/j.compscitech.2021.108963.

[6] F. Ram, J. Garemark, Y. Li, L. Berglund, Scalable, efficient piezoelectric wood nanogenerators enabled by wood/ZnO nanocomposites, Compos. Part A Appl. Sci. Manuf. 160 (2022), https://doi.org/10.1016/j.compositesa.2022.107057.

[7] J. Sun, K. Tu, S. Büchele, S.M. Koch, Y. Ding, S.N. Ramakrishna, S. Stucki, H. Guo, C. Wu, T. Keplinger, J. Pérez-Ramírez, I. Burgert, G. Panzarasa, Functionalized wood with tunable tribopolarity for efficient triboelectric nanogenerators, Matter. 4 (2021) 3049–3066, https://doi.org/10.1016/j.matt.2021.07.022.

[8] F. Eiichi, Piezoelectricity as a fundamental property of wood, Wood Sci. Technol. 2 (1968) 299–307, https://doi.org/10.1007/BF00350276.

[9] M.H. Shamos, L.S. Lavine, Piezoelectricity as a Fundamental Property of Biological Tissues, Nature 213 (1967) 267–269, https://doi.org/10.1038/213267a0.

[10] J. Sun, H. Guo, G.N. Schädli, K. Tu, S. Schär, F.W.M.R. Schwarze, G. Panzarasa, J. Ribera, I. Burgert, Enhanced mechanical energy conversion with selectively decayed wood, Sci. Adv. 7 (2021). http://advances.sciencemag.org/.

[11] L.A. Berglund, I. Burgert, Bioinspired Wood Nanotechnology for Functional Materials, Adv. Mater. 30 (2018), https://doi.org/10.1002/adma.201704285.

[12] Z.L. Wang, Zinc oxide nanostructures: Growth, properties and applications, J. Phys. Condens. Matter 16 (2004), https://doi.org/10.1088/0953-8984/16/25/R01.

[13] Y. Dong, Y. Yan, H. Ma, S. Zhang, J. Li, C. Xia, S.Q. Shi, L. Cai, In-Situ Chemosynthesis of ZnO Nanoparticles to Endow Wood with Antibacterial and UV-Resistance Properties, J. Mater. Sci. Technol. 33 (2017) 266–270, https://doi.org/10.1016/j.jmst.2016.03.018.

[14] Z. Liu, T. Fan, D. Zhang, X. Gong, J. Xu, Hierarchically porous ZnO with high sensitivity and selectivity to H 2 S derived from biotemplates, Sens. Actuators B Chem. 136 (2009) 499–509, https://doi.org/10.1016/j.snb.2008.10.043.

[15] Y. Wang, T. Tian, E. Cabane, Wood Composites with Wettability Patterns Prepared by Controlled and Selective Chemical Modification of a Three-Dimensional Wood Scaffol, ACS Sustain. Chem. Eng. 5 (2017) 11686–11694, https://doi.org/10.1021/acssuschemeng.7b03104.

[16] M. Höglund, J. Garemark, M. Nero, T. Willhammar, S. Popov, L.A. Berglund, Facile Processing of Transparent Wood Nanocomposites with Structural Color from Plasmonic Nanoparticles, Chem. Mater. 33 (2021) 3736–3745, https://doi.org/10.1021/acs.chemmater.1c00806.

[17] M. Zhou, D. Zang, X. Zhai, Z. Gao, W. Zhang, C. Wang, Preparation of biomorphic porous zinc oxide by wood template method, Ceram. Int. 42 (2016) 10704–10710, https://doi.org/10.1016/j.ceramint.2016.03.188.

[18] H. Schreier, J.J. Orteu, M.A. Sutton, Image correlation for shape, motion and deformation measurements: Basic concepts, theory and applications, Springer, US (2009), https://doi.org/10.1007/978-0-387-78747-3.

[19] B. Pan, Digital image correlation for surface deformation measurement: Historical developments, recent advances and future goals, Meas. Sci. Technol. 29 (2018), https://doi.org/10.1088/1361-6501/aac55b.

[20] J. Sirvio, U. Hyvakko, H. Liimatainen, J. Niinimaki, O. Hormi, Periodate oxidation of cellulose at elevated temperatures using metal salts as cellulose activators, Carbohydr. Polym. 83 (2011) 1293–1297, https://doi.org/10.1016/j.carbpol.2010.09.036.

[21] L. Segal, J.J. Creely, A.E. Martin, C.M. Conrad, An Empirical Method for Estimating the Degree of Crystallinity of Native Cellulose Using the X-Ray Diffractometer, Text. Res. J. 29 (1959) 786–794, https://doi.org/10.1177/004051755902901003.

[22] M.E. Karlsson, Y.C. Mamie, A. Calamida, J.M. Gardner, V. Ström, A.M. Pourrahimi, R.T. Olsson, Synthesis of Zinc Oxide Nanorods via the Formation of Sea Urchin Structures and Their Photoluminescence after Heat Treatment, Langmuir 34 (2018) 5079–5087, https://doi.org/10.1021/acs.langmuir.8b01101.

[23] Y. Li, Q. Fu, R. Rojas, M. Yan, M. Lawoko, L. Berglund, Lignin-Retaining Transparent Wood, ChemSusChem. 10 (2017) 3445–3451, https://doi.org/10.1002/cssc.201701089.

[24] J. Chen, Z. Zhu, H. Zhang, S. Fu, Superhydrophobic light-driven actuator based on self-densified wood film with a sandwich-like structure, Compos. Sci. Technol. 220 (2022), https://doi.org/10.1016/j.compscitech.2022.109278.

[25] Y. Gao, M. del, C. Aliques Tomas, J. Garemark, X. Sheng, L. Berglund, Y. Li, Olive Stone Delignification Toward Efficient Adsorption of Metal Ions, Front Mater. 8 (2021), https://doi.org/10.3389/fmats.2021.605931.

[26] V. López Durán, P.A. Larsson, L. Wågberg, On the relationship between fibre composition and material properties following periodate oxidation and borohydride reduction of lignocellulosic fibres, Cellulose 23 (2016) 3495–3510, https://doi.org/10.1007/s10570-016-1061-4.

[27] C.B. Ong, L.Y. Ng, A.W. Mohammad, A review of ZnO nanoparticles as solar photocatalysts: Synthesis, mechanisms and applications, Renew. Sustain. Energy Rev. 81 (2018) 536–551, https://doi.org/10.1016/j.rser.2017.08.020.

[28] T. Demes, C. Ternon, F. Morisot, D. Riassetto, M. Legallais, H. Roussel, M. Langlet, Mechanisms involved in the hydrothermal growth of ultra-thin and high aspect ratio ZnO nanowires, Appl. Surf. Sci. 410 (2017) 423–431, https://doi.org/10.1016/j.apsusc.2017.03.086.

[29] C.L. Chengyu Wang, C. Piao, Synthesis and Characterization of Superhydrophobic Wood Surfaces, J. Appl. Polym. Sci. 116 (2010) 2658–2667, https://doi.org/10.1002/app.

[30] Q. Sun, Y. Lu, H. Zhang, D. Yang, Y. Wang, J. Xu, J. Tu, Y. Liu, J. Li, Improved UV resistance in wood through the hydrothermal growth of highly ordered ZnO nanorod arrays, J. Mater. Sci. 47 (2012) 4457–4462, https://doi.org/10.1007/s10853-012-6304-7.

[31] S.W. Bian, I.A. Mudunkotuwa, T. Rupasinghe, V.H. Grassian, Aggregation and dissolution of 4 nm ZnO nanoparticles in aqueous environments: Influence of pH, ionic strength, size, and adsorption of humic acid, Langmuir 27 (2011) 6059–6068, https://doi.org/10.1021/la200570n.

[32] F. Ram, B. Biswas, A. Torris, G. Kumaraswamy, K. Shanmuganathan, Elastic piezoelectric aerogels from isotropic and directionally ice-templated cellulose nanocrystals: comparison of structure and energy harvesting, Cellulose 28 (2021) 6323–6337, https://doi.org/10.1007/s10570-021-03896-6.

[33] M.J. Moody, C.W. Marvin, G.R. Hutchison, Molecularly-doped polyurethane foams with massive piezoelectric response, J. Mater. Chem. C Mater. 4 (2016) 4387–4392, https://doi.org/10.1039/c6tc00613b.

[34] F. Ram, K. Suresh, A. Torris, G. Kumaraswamy, K. Shanmuganathan, Highly compressible ceramic/polymer aerogel-based piezoelectric nanogenerators with enhanced mechanical energy harvesting property, Ceram. Int. 47 (2021) 15750–15758, https://doi.org/10.1016/j.ceramint.2021.02.147.

[35] M.F. Ashby, R.F. Mehl Medalist, The mechanical properties of cellular solids, Metall. Mater. Trans. A 14 (1983) 1755–1769, https://doi.org/10.1007/BF02645546.

[36] S. Xu, Z.L. Wang, One-dimensional ZnO nanostructures: Solution growth and functional properties, Nano Res. 4 (2011) 1013–1098, https://doi.org/10.1007/s12274-011-0160-7.